PHYSICAL REVIEW B **96**, 081410(R) (2017)

Large optical conductivity of Dirac semimetal Fermi arc surface states

Li-kun Shi[1] and Justin C. W. Song[1,2,*]

[1]*Institute of High Performance Computing, Agency for Science, Technology and Research, Singapore 138632*

[2]*Division of Physics and Applied Physics, Nanyang Technological University, Singapore 637371*

(Received 8 May 2017; revised manuscript received 15 July 2017; published 30 August 2017)

Fermi arc surface states, a hallmark of topological Dirac semimetals, can host carriers that exhibit unusual dynamics distinct from that of their parent bulk. Here we find that Fermi arc carriers in intrinsic Dirac semimetals possess a strong and anisotropic light-matter interaction. This is characterized by a large Fermi arc optical conductivity when light is polarized transverse to the Fermi arc; when light is polarized along the Fermi arc, Fermi arc optical conductivity is significantly muted. The large surface spectral weight is locked to the wide separation between Dirac nodes and persists as a large Drude weight of Fermi arc carriers when the system is doped. As a result, large and anisotropic Fermi arc conductivity provides a novel means of optically interrogating the topological surfaces states of Dirac semimetals.

DOI: 10.1103/PhysRevB.96.081410

Three-dimensional (3D) topological Dirac semimetals (DSMs) possess fourfold degenerate band touchings in the bulk (Dirac points) that are stabilized by the underlying crystal symmetries [1–3]. Of special interest are the unusual surface states in DSMs, which are localized on particular exposed crystal surfaces even in the presence of bulk metallic states. These Fermi arc surface states feature several interesting properties including spin-momentum locking [3,4], and possess a dispersion that spans the large expanse of momenta between the Dirac nodes [Fig. 1(a)] [3–13]. As a result, carriers on the Fermi arc surface states exhibit markedly different dynamics from that of carriers in the bulk—a hallmark of the unconventional fermiology of DSMs [14,15].

Here we argue that Fermi arc surface states in DSMs can mediate a large optical response. In particular, for an undoped DSM with Dirac nodes at $k_z = \pm k_0$ (Fig. 1), we find that the interband optical conductivity associated with optical absorption in Fermi arc surface states can attain large values of several tens of e^2/h when incident light is polarized along the $\hat{\mathbf{x}}$ direction [Fig. 2(a)]. These values are far larger than those of other gapless two-dimensional (2D) electron gases (e.g., undoped graphene [16]). Further, interband optical conductivity displays a distinctive peaklike frequency dependence which does not vanish at small frequencies [Fig. 2(a)] arising from the double-arch-shaped dispersion of the DSM Fermi arc states (Fig. 1). This contrasts with the vanishing optical conductivity expected from the DSM bulk [17].

Large DSM surface absorption along $\hat{\mathbf{x}}$ stems from the wide range of momenta between $-k_0 < k_z < k_0$ that DSM Fermi arc surface states span. As a result, a large set of particle-hole transitions occur, leading to large surface absorption values. Additionally, since DSM Fermi arc surface states arise from a band inversion between bands of different parity, they possess a canted spin texture. As we explain below, this spin texture mediates contrasting optical selection rules for interband electron-hole transitions when incident light is polarized in $\hat{\mathbf{x}}$ or $\hat{\mathbf{z}}$ directions: when incident light is polarized along $\hat{\mathbf{z}}$, absorption resulting from transitions between Fermi arc surface states can be 100–1000 times smaller (than along $\hat{\mathbf{x}}$), displaying a strong anisotropy [Fig. 2(b)].

In doped DSMs, the large values of DSM surface absorption persists in the form of a Drude weight along $\hat{\mathbf{x}}$ giving a large intraband (Drude) absorption. The total optical weight for both intra- and interband absorption along x is conserved and we obtain an explicit expression for the spectral weight that is directly dependent on the separation between the Dirac nodes, $2k_0$. The distinctive qualitative features of DSM surface absorption departs from that of the bulk, and provides an optical means of probing the dynamics of the Fermi arc surface state carriers.

Effective Hamiltonian and surface states. We begin by considering three-dimensional topological DSMs [1,2,12] which possess rotational symmetry along the k_z axis, and a pair of Dirac points at $\pm\mathbf{k}_0 = (0,0,\pm k_0)$ within the Brillouin zone [3–11]. These can be described by a minimal 4×4 Hamiltonian [1,2,12], $\mathcal{H} = \mathcal{H}_0 + \mathcal{H}'$ with

$$\mathcal{H}_0 = m_{\mathbf{k}}\mathbf{s}_0\boldsymbol{\tau}_3 + v(k_x\mathbf{s}_3\boldsymbol{\tau}_1 - k_y\mathbf{s}_0\boldsymbol{\tau}_2), \tag{1}$$

where $\mathbf{k} = (k_x,k_y,k_z)$ is taken about the $\Gamma_{3D} = (0,0,0)$ point, $\mathbf{s}_0$ ($\boldsymbol{\tau}_0$) is an identity matrix, $\mathbf{s}_{1,2,3}$ ($\boldsymbol{\tau}_{1,2,3}$) are Pauli matrices representing the spin (orbital) degrees of freedom, and $\mathcal{H}' \sim O(k^3)$ is a higher-order term (see below). Here, the mass takes the form $m_{\mathbf{k}} = -m_0 + m_1 k_z^2$ along the k_z axis, with $m_0 > 0$

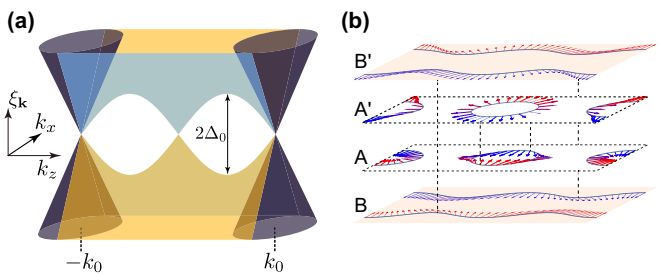

FIG. 1. (a) Schematic dispersion for surface states (blue and yellow) between the Dirac cones (purple) in three-dimensional topological Dirac semimetals; surface is terminated normal to $\hat{\mathbf{y}}$. Upper and lower branches of surface states are degenerate at $(k_x,k_z) = 0$ and at the Dirac points $(k_x,k_z) = (0,\pm k_0)$, while gapped elsewhere with gap characterized by $\Delta_{\mathbf{k}_{2D}}$ (see text). (b) Particle-hole excitation between surface states at different energies. Transitions from $A \to A'$ ($B \to B'$) correspond to photon energy $\hbar\omega < 2\Delta_0$ ($\hbar\omega > 2\Delta_0$). Red and blue arrows display the spin textures.

*justinsong@ntu.edu.sg

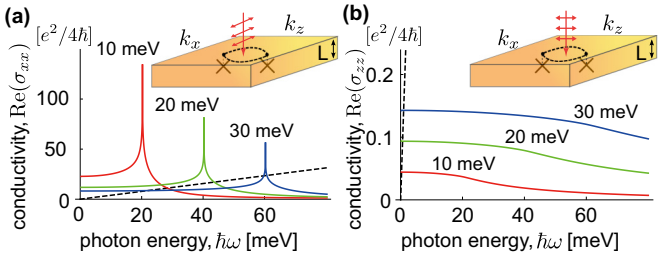

FIG. 2. Real part of interband conductivity $\mathrm{Re}(\sigma_{xx})$ [solid lines in (a)] and $\mathrm{Re}(\sigma_{zz})$ [solid lines in (b)] from inter-Fermi arc state transitions obtained from Eq. (11) at $\mu = 0$ per surface. For comparison, bulk interband transitions for a $L_y = 500$ nm thin slab—measured by an effective 2D conductance: bulk conductivity multiplied by L_y—are shown in dashed lines (see [17,18] for detailed calculations). We have chosen units $e^2/4\hbar$ for the optical conductivity of graphene as a reference. Parameters used: $v = 450$ meV nm ($\approx 6.9 \times 10^5$ m s^{-1}), $k_0 = 1.5$ nm^{-1}, bulk carrier velocity $A_x = v$, and $A_z = 250$ meV nm ($\approx 3.8 \times 10^5$ m s^{-1}). Red, green, and blue correspond to $\Delta_0 = 10$, 20, and 30 meV, respectively.

capturing band inversion [1,2] between the Dirac points $\pm k_0 = \pm\sqrt{m_0/m_1}$.

Since $\mathcal{H}_0$ in Eq. (1) possesses only diagonal $\mathbf{s}_0,\mathbf{s}_3$ terms, $\mathcal{H}_0$ is block diagonal in spin space; the pair of 2×2 blocks (denoted $s = \pm 1$) are related via time-reversal symmetry (TRS) [1,2,4]. In contrast, $\mathcal{H}'$ is purely off-diagonal, coupling the $s = \pm 1$ blocks. Further, it is weak with $\mathcal{H}' = \alpha k_z[(k_x^2 - k_y^2)\mathbf{s}_1\boldsymbol{\tau}_1 - k_x k_y \mathbf{s}_2\boldsymbol{\tau}_1]$ [1], and vanishes along the k_z axis due to rotational symmetry (RS) [1–3]; α determines the magnitude of the high-order term $\mathcal{H}'$ [1]. As a result, a pair of degenerate Dirac nodes emerge at $\pm\mathbf{k}_0$ where scattering between $s = +1$ and $s = -1$ blocks vanish. $\mathcal{H}$ captures the essential low-energy physics of DSMs, and has been recently used to describe several DSM systems including Na_3Bi and Cd_3As_2 [8,9], which have threefold and fourfold rotational symmetries, respectively.

Of particular interest are surface states that develop on certain exposed surfaces due to the band inversion of conduction and valence bands between the Dirac nodes. To illustrate these states, we will consider a DSM in the region $y \geqslant 0$ described by Eq. (1); vacuum occupies $y < 0$. For each fixed $\mathbf{k}_{2D} = (k_x,k_z)$ between the Dirac points projected onto the x-z plane, each block $s = \pm 1$ of Eq. (1) describes a one-dimensional Dirac system with a sign changing mass as a function of y [2,12]. As a result, Jackiw-Rebbi type surface states emerge, and are localized about $y = 0$ with wave function

$$\Psi^{\mathrm{surf}}_{\mathbf{k}_{2D},s}(y) = \langle y|\Psi^{\mathrm{surf}}_{\mathbf{k}_{2D},s}\rangle = C_{\mathbf{k}_{2D}} e^{-y/\lambda_{\mathbf{k}_{2D}}} u_s, \tag{2}$$

where $u_{s=+1} = (1,1,0,0)^T$, $u_{s=-1} = (0,0,1,1)^T$, decay length $\lambda_{\mathbf{k}_{2D}} = -v/m_{\mathbf{k}_{2D}} > 0$ [18], and $C_{\mathbf{k}_{2D}}$ is a normalization constant; we have suppressed the plane wave part for brevity. Here u_s are $\mathbf{k}_{2D}$-independent block spinors arising from the $s = \pm 1$ block in Eq. (1), respectively [18]. The surface states in Eq. (2) only exist between $k_z = \pm k_0$ due to wave-function normalizability [18]. Indeed, when $k_z \to \pm k_0$, $\lambda_{\mathbf{k}_{2D}}$ diverges, indicating that $\Psi_{\mathbf{k}_{2D},s}(y)$ merges into the bulk.

Using the surface states in Eq. (2) as a basis $\{\Psi^{\mathrm{surf}}_{\mathbf{k}_{2D},s=+1}, \Psi^{\mathrm{surf}}_{\mathbf{k}_{2D},s=-1}\}$, we write a Hamiltonian describing the surface electronic behavior as

$$\mathcal{H}_{\mathrm{surf}} = v k_x \boldsymbol{\sigma}_z + \Delta_{\mathbf{k}_{2D}} \boldsymbol{\sigma}_x, \tag{3}$$

and can be obtained directly from Eq. (1); for a full discussion of this procedure, see [18]. The first term describes the linear dispersion of the surface states, whereas the second term describes interblock mixing.

The eigenfunctions of Eq. (3) can be readily obtained as spinors $\psi^+_{\mathbf{k}_{2D}} = [\sin(\phi_{\mathbf{k}_{2D}}/2), \cos(\phi_{\mathbf{k}_{2D}}/2)]$ and $\psi^-_{\mathbf{k}_{2D}} = [\cos(\phi_{\mathbf{k}_{2D}}/2), -\sin(\phi_{\mathbf{k}_{2D}}/2)]$, with energy eigenvalue $\xi^{\pm}_{\mathbf{k}_{2D}} = \pm\eta_{\mathbf{k}_{2D}}$, where $\tan\phi_{\mathbf{k}_{2D}} = \Delta_{\mathbf{k}_{2D}}/vk_x$ [19] and $\eta_{\mathbf{k}_{2D}} = (\Delta^2_{\mathbf{k}_{2D}} + v^2k_x^2)^{1/2}$. Each of the components of $\psi_{\mathbf{k}_{2D}}$ denote the wave-function weight on the $s = \pm 1$ blocks, respectively. These surface states can be probed directly via angle-resolved photoemission spectroscopy [3–8]. Additionally, carriers moving along DSM states may also exhibit peculiar cyclotron orbits [14] and can be probed via quantum oscillations [15].

Crucially, the spin blocks $s = \pm 1$ decouple at zero nodes of $\Delta_{\mathbf{k}_{2D}}$ as governed by the symmetries of the system. For example, at $\mathbf{k}_{2D} = (k_x,k_z) = 0$, $\Delta(\mathbf{k}_{2D} = 0)$ vanishes since $|\Psi^{\mathrm{surf}}_{\mathbf{k}_{2D}=0,s}\rangle$ and $|\Psi^{\mathrm{surf}}_{\mathbf{k}_{2D}=0,-s}\rangle$ are a Kramers pair related by TRS [2,13]. For an explicit discussion of this, see [18]. Further, we note that in a pristine system without surface potentials coupling the spin blocks [18], $\Delta_{\mathbf{k}_{2D}}$ also vanishes at the two projected Dirac points $\pm\mathbf{k}^{\mathrm{Dirac}}_{2D} = (0,k_z = \pm k_0)$ [14,18]. This is because the surface state wave function delocalizes fully into the bulk at the two projected Dirac points $\mathbf{k}^{\mathrm{Dirac}}_{2D}$. As a result, RS about the k_z axis of the *bulk* Hamiltonian (which protects the bulk 3D Dirac points) also determines the degeneracies of the surface states at the two projected $\mathbf{k}^{\mathrm{Dirac}}_{2D}$ [14,18]. We note, parenthetically, that in nonideal systems, nonrotationally symmetric surface potentials can gap out the nodes at $\pm\mathbf{k}^{\mathrm{Dirac}}_{2D}$. However, the zero node at $\mathbf{k}_{2D} = 0$ is robust against disorder/potentials that preserve TRS allowing the qualitative features of the Fermi arc conductivity we discuss below to persist.

Inter-Fermi arc transitions. As we now show, DSM surface states in Eq. (3) exhibit a strong light-matter interaction. In the presence of normally incident light $\boldsymbol{\mathcal{E}} = \mathbf{E}\cos\omega t$ on the exposed surface, electron-hole transitions occur between the occupied and unoccupied surface states [Figs. 1(a) and 1(b)]. These can be described via the standard golden rule technique as

$$W = \frac{2\pi}{\hbar}\sum_{\mathbf{k}_{2D}} |M_{\mathbf{k}_{2D}}|^2 \delta(\xi^+_{\mathbf{k}_{2D}} - \xi^-_{\mathbf{k}_{2D}} - \hbar\omega) f(\xi^-_{\mathbf{k}_{2D}})[1 - f(\xi^+_{\mathbf{k}_{2D}})], \tag{4}$$

where $f(x) = [e^{(x-\mu)/k_BT} + 1]^{-1}$ is the Fermi function, with μ the chemical potential.

For clarity, we adopt a simplified phenomenological model for $\Delta_{\mathbf{k}_{2D}} = \Delta_0 \sin(\pi k_z/k_0)$ in Eq. (3) which respects the symmetries of the system. This choice of $\Delta_{\mathbf{k}_{2D}}$ captures the zero nodes at $\mathbf{k}_{2D} = 0$, as well as the two projected Dirac nodes at $\pm\mathbf{k}^{\mathrm{Dirac}}_{2D} = (0,k_z = \pm k_0)$ [18]. We note that other models for $\Delta_{\mathbf{k}_{2D}}$ can also be used; however, we do not expect them to alter the qualitative conclusions discussed below (see, e.g., [18] for a discussion of other models). Writing $\mathbf{k}_{2D} \to \mathbf{k}_{2D} - e\boldsymbol{\mathcal{A}}/\hbar c$ in Eq. (3), with the vector potential satisfying $\boldsymbol{\mathcal{E}} = (1/c)\partial_t\boldsymbol{\mathcal{A}}$

and expanding to linear order in $\mathbf{E}$ yields the matrix elements

$$M_{\mathbf{k}_{2D}} = \frac{ie}{2\hbar\omega}\langle\psi^{+}_{\mathbf{k}_{2D}}|v_x E_x \boldsymbol{\sigma}_z + v_z \cos(\pi k_z/k_0) E_z \boldsymbol{\sigma}_x|\psi^{-}_{\mathbf{k}_{2D}}\rangle, \tag{5}$$

where $v_x = v$, and $v_z = \pi\Delta_0/k_0$.

Particle-hole excitations occur on the equienergy contours defined by $\eta_{\mathbf{k}_{2D}} = \hbar\omega/2$ in k space since energy conservation demands $\delta(\xi^{+}_{\mathbf{k}_{2D}} - \xi^{-}_{\mathbf{k}_{2D}} - \hbar\omega) = \delta(2\eta_{\mathbf{k}_{2D}} - \hbar\omega)$. These contours can be classified into two types: (A) $\hbar\omega < 2\Delta_0$ wherein particle-hole excitations occur along contours with multiple disconnected segments [see Fig. 1(b)], and (B) $\hbar\omega > 2\Delta_0$ where particle-hole excitations occur along two long singly connected arcs [the so-called "Fermi arcs"; see Fig. 1(b)]. When $\hbar\omega = 2\Delta_0$, the particle-hole excitations transform from A- to B-type contours.

In order to keep track of the distinct topologies of A- and B-type contours, it will be convenient to define the particle-hole excitation spectrum as

$$\rho(\omega,\nu) = \int_0^\infty R(\eta,\nu)\delta(2\eta - \hbar\omega)d\eta, \quad R = \left|\frac{\partial(k_x,k_z)}{\partial(\eta,\nu)}\right|, \tag{6}$$

with $\nu(\mathbf{k}_{2D}) = \phi_{\mathbf{k}_{2D}}$ for $\hbar\omega < 2\Delta_0$ describing A-type contours, and $\nu(\mathbf{k}_{2D}) = \pi k_z/k_0$ for $\hbar\omega \geqslant 2\Delta_0$ denoting B-type contours; in both cases $-\pi < \nu < \pi$. This choice of $\nu(\mathbf{k}_{2D})$ results in simple forms for the Jacobian: $R(\eta,\nu) = 2D(\eta/\Delta_0)[1 - (\eta/\Delta_0)^2 \sin^2\nu]^{-1/2}$ for A-type contours ($\hbar\omega < 2\Delta_0$), and $R(\eta,\nu) = 2D[1 - (\Delta_0/\eta)^2\sin^2\nu]^{-1/2}$ for B-type contours ($\hbar\omega \geqslant 2\Delta_0$), where $D = (2\pi)^{-2}(\Delta_0/v_x v_z)$ [18].

Using Eq. (6), we can write the transition rate, Eq. (4), in a compact form

$$W(\omega) = \frac{2\pi}{\hbar}\int_{-\pi}^{\pi} d\nu|\mathcal{M}(\omega,\nu)|^2\rho(\omega,\nu)f(\xi^{-})[1 - f(\xi^{+})], \tag{7}$$

where the matrix elements $\mathcal{M} = \mathcal{M}_x + \mathcal{M}_z$ are

$$\mathcal{M}_x = \frac{eE_x}{2\hbar\omega}\frac{v_x \sin\nu}{\bar{\omega}^{(1/2)(1+\zeta)}}, \quad \mathcal{M}_z = \frac{eE_z}{2\hbar\omega}\frac{v_z\cos\nu}{(1 - \bar{\omega}^{-2\zeta}\sin^2\nu)^{-1/2}}, \tag{8}$$

where $\bar{\omega} = \hbar\omega/2\Delta_0$, and we have noted $\langle\psi^{+}_{\mathbf{k}_{2D}}|\boldsymbol{\sigma}_x|\psi^{-}_{\mathbf{k}_{2D}}\rangle = \cos\phi_{\mathbf{k}_{2D}}$ and $\langle\psi^{+}_{\mathbf{k}_{2D}}|\boldsymbol{\sigma}_z|\psi^{-}_{\mathbf{k}_{2D}}\rangle = \sin\phi_{\mathbf{k}_{2D}}$. Here $\zeta(\bar{\omega}) = \mathrm{sgn}(\bar{\omega} - 1)$ tracks the A-type (where $\zeta = -1$) and B-type (where $\zeta = 1$) contours that determine the particle-hole excitations. Performing the integral in Eq. (6), we obtain

$$\rho(\omega,\nu) = \frac{1}{2\pi^2}\frac{\Delta_0}{v_x v_z}\frac{\bar{\omega}^{(1/2)(1-\zeta)}}{(1 - \bar{\omega}^{-2\zeta}\sin^2\nu)^{1/2}}. \tag{9}$$

As we will see below, the distinct angular features of both $\mathcal{M}$ and ρ lead to a large anisotropy in the interband absorption spectrum when the incident light field is polarized along $\hat{\mathbf{x}}$ vs $\hat{\mathbf{z}}$.

Using Ohms' law, $\hbar\omega W(\omega) = \mathrm{Re}\,[\sigma(\omega)]|\mathbf{E}|^2/2$, and Eq. (7) we obtain the interband conductivity for $\boldsymbol{\mathcal{E}}$ polarized along $\hat{\mathbf{x}}$ and $\hat{\mathbf{z}}$ directions as

$$\mathrm{Re}[\sigma_{ii}(\omega)] = (e^2/\hbar)\chi_{ii}(\omega)\Theta(\hbar\omega/2 - |\mu|) \quad (i = x,z), \tag{10}$$

where we have approximated $f(\xi^{-})[1 - f(\xi^{+})] = f(-\hbar\omega/2)[1 - f(\hbar\omega/2)] = \Theta(\hbar\omega/2 - |\mu|)$ at low temperatures $k_B T \ll \hbar\omega/2$. Here $\chi_{xx}(\omega)$ and $\chi_{zz}(\omega)$ (the dynamical conductivity at $\mu = 0$) are

$$\chi_{xx}(\omega) = \frac{v_x}{v_z}I_x(\omega), \quad \chi_{zz}(\omega) = \frac{v_z}{v_x}I_z(\omega), \tag{11}$$

where $I_x(\omega) = \frac{\bar{\omega}^{-(3/2)(1+\zeta)}}{4\pi}\int_{-\pi}^{\pi}(1 - \bar{\omega}^{-2\zeta}\sin^2\nu)^{-1/2}\sin^2\nu d\nu$, and $I_z(\omega) = \frac{\bar{\omega}^{-(1/2)(1+\zeta)}}{4\pi}\int_{-\pi}^{\pi}(1 - \bar{\omega}^{-2\zeta}\sin^2\nu)^{1/2}\cos^2\nu d\nu$.

Plotting Eqs. (11) and (10) in Fig. 2(a) we find a large Fermi arc interband optical conductivity $\mathrm{Re}(\sigma_{xx})$ per surface when light is polarized along $\hat{\mathbf{x}}$ (for parameters, see caption). Indeed, even at relatively low frequencies, $\mathrm{Re}(\sigma_{xx})$ can be up to 20 times that found in monolayer graphene [16]. Strikingly, for frequencies approaching $\hbar\omega = 2\Delta_0$, surface $\mathrm{Re}(\sigma_{xx})$ diverges. This peak structure in the frequency dependence of $\mathrm{Re}(\sigma_{xx})$ arises from a Van Hove singularity when the particle-hole spectrum transitions between A- and B- type contours [Figs. 1(a) and 1(b)]. Its frequency dependence contrasts with the linear frequency dependence of DSM bulk interband optical conductivity which vanishes at low frequency [17]. Since bulk absorption directly scales with DSM film thickness, the contribution of Fermi arc optical conductivity (insensitive to film thickness) can be extracted in a thickness dependence study of optical absorption.

At low frequencies, $\mathrm{Re}(\sigma_{xx})$ can even dominate over absorption in the bulk for moderately thin-slab samples. For illustration, we note that the effective 2D optical conductivity in DSM slabs contributed from the bulk—the bulk conductivity multiplied by thickness of the sample—can be written as $\mathrm{Re}\,[G^{\mathrm{bulk}}_{xx}(\omega)] = (e^2/\hbar)(1/12\pi)(\hbar\omega L_y/A_z)\Theta(\hbar\omega/2 - \mu)$ [17,18]. $\mathrm{Re}\,[G^{\mathrm{bulk}}_{xx}(\omega)]$ is linearly dependent on the thickness L_y; A_z is the bulk carrier velocity [3,8,11]. Taking $L_y =$ 500 nm, for example, we find that $\mathrm{Re}(\sigma_{xx})$ per surface (solid line) overwhelms that of the bulk (dashed line) at low frequencies [Fig. 2(a)].

For light polarized in the $\hat{\mathbf{z}}$ direction, the Fermi arc interband optical conductivity $\mathrm{Re}(\sigma_{zz})$ [Fig. 2(b)] exhibits a significantly muted magnitude and frequency dependence from that found for $\mathrm{Re}(\sigma_{xx})$. To understand this we note that the ratio between χ_{xx}/χ_{zz} scales as the square of their velocities $(v_x/v_z)^2 = (vk_0/\pi\Delta_0)^2$ [see Eq. (11)], yielding a large ratio between $\chi_{xx}/\chi_{zz} \sim$ 100–1000. This produces small $\mathrm{Re}(\sigma_{zz})$ values and a linear dichroism for transitions between Fermi arc states [20]. In contrast to $\mathrm{Re}(\sigma_{xx})$ above, we find that bulk interband optical conductivity (dashed line) prevails over surface Fermi arc (solid lines) when light is polarized along $\hat{\mathbf{z}}$ [Fig. 2(b)].

We note that the presence/absence of rotational symmetry on the surface can alter the nodal structure close to the projected Dirac points at $k_z = \pm k_0$; when rotational symmetry on the surface is broken, the nodes at $k_z = \pm k_0$ are gapped out. However, the node at $\mathbf{k}_{2D} = 0$ is protected by TRS. As a result, we expect the qualitative features of $\mathrm{Re}(\sigma_{xx})$ to persist even when rotational symmetry on the surface is broken (see [18] for discussion).

Fermi arc intraband conductivity. At finite chemical potential, $\mu \neq 0$, low frequency optical transitions described in Eq. (10) are Pauli blocked. As we now argue, the large conductivity along $\hat{\mathbf{x}}$ persists in the Drude conductivity. We

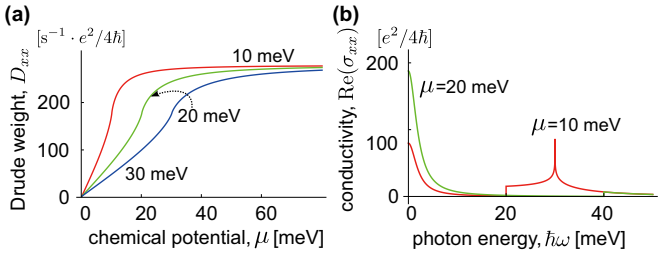

FIG. 3. (a) Drude weight D_{xx} obtained from Eq. (13), with parameters used the same as Fig. 2. (b) Real part of conductivity σ_{xx}, including both inter- and intraband parts, at different chemical potentials μ, where we have used $\Delta_0 = 15$ meV and scattering time $\tau = 10$ ps for illustration.

capture this by a simple Drude model

$$\sigma^{\mathrm{D}}_{xx}(\omega) = \frac{D_{xx}}{-i\omega + 1/\tau}, \quad D_{xx} = -e^2 \sum_{\mathbf{k}_{2\mathrm{D}}} u^2_{\mathbf{k}x} \frac{\partial f(\xi_{\mathbf{k}_{2\mathrm{D}}})}{\partial \xi_{\mathbf{k}_{2\mathrm{D}}}}, \quad (12)$$

where τ is the scattering time, and D_{xx} is the Drude weight. Here $u_{\mathbf{k}x} = \langle \psi_{\mathbf{k}_{2\mathrm{D}}} | \partial \mathcal{H}_{\mathrm{surf}}/\partial(\hbar k_x) | \psi_{\mathbf{k}_{2\mathrm{D}}} \rangle$ is the band velocity in the $\hat{\mathbf{x}}$ direction.

For the degenerate limit, $k_B T \ll \mu$ at low temperatures, we use $[-\partial f(\xi^{\alpha}_{\mathbf{k}_{2\mathrm{D}}})/\partial \xi_{\mathbf{k}_{2\mathrm{D}}}] = \delta(\eta_{\mathbf{k}_{2\mathrm{D}}} - \mu)$. Following the same procedure above in Eqs. (6)–(11), we obtain

$$D_{xx} = \frac{e^2}{\hbar} \frac{v_x}{v_z} \frac{2\Delta_0}{\pi\hbar} \mathcal{I}_x(\mu), \qquad \bar{\mu} = \mu/\Delta_0, \quad (13)$$

where $\mathcal{I}_x(\mu) = \frac{\bar{\mu}^{(1-\zeta)/2}}{4\pi} \int_{-\pi}^{\pi} [1 - \bar{\mu}^{-(1+\zeta)} \sin^2 \nu]/[1 - \bar{\mu}^{-2\zeta} \sin^2 \nu]^{1/2} d\nu$, and $\zeta(\bar{\omega}) = \mathrm{sgn}(\bar{\omega} - 1)$ as defined in Eq. (8). Here we have used $(u_{\mathbf{k}x})^2 = (v_x/\hbar)^2 \cos^2 \phi_{\mathbf{k}_{2\mathrm{D}}}$.

In Fig. 3(a), we plot the Drude weight obtained from Eq. (13) as a function of μ. The Drude weight increases sharply from $\mu = 0$, and saturates to a large value $D_{xx} \to D_0 = (e/\pi\hbar)^2 v_x k_0$ for $\bar{\mu} \gg 1$. Here we have noted that $\mathcal{I}_x(\mu \to +\infty) \to 1/2$. Interestingly, the large saturated value D_0 is independent of Δ_0, and depends directly on the distance between the Dirac nodes, k_0.

Large values of k_0 are also responsible for the strong interband optical conductivity along $\hat{\mathbf{x}}$ described above [see Eq. (11)]. Indeed, directly summing the Drude and the interband conductivities along $\hat{\mathbf{x}}$ in Eqs. (11) and (13), we obtain an approximate partial sum rule

$$\int_0^{\Omega} \mathrm{Re}\left[\sigma^{D}_{xx}(\omega)\right] d\omega + \int_0^{\Omega} \mathrm{Re}\left[\sigma_{xx}(\omega)\right] d\omega = \mathcal{S}, \quad (14)$$

where we have taken $\Omega \gg 1/\tau, \hbar/\Delta_0, \hbar/\mu$, and $\mathcal{S} = (e^2/\hbar)(v_x k_0/2\pi\hbar)$ is a constant that depends on k_0, the distance between the Dirac nodes. In obtaining the value of $\mathcal{S}$, we have noted that $\int_0^{\Omega} \mathrm{Re}\left[\sigma_{xx}(\omega)\right] d\omega = c \int_{2\mu}^{\Omega} I_x(\mu') d\mu' = c\Delta_0[\mathcal{I}_x(\Omega/2) - \mathcal{I}_x(\mu)]$, where $c = (e^2/\hbar^2)(v_x/v_z)$. In the last line, we have used $\partial_\mu \mathcal{I}_x(\mu) = \Delta_0^{-1} I_x(2\mu)$ [18]. We also noted that the frequency integral of the intraband conductivity yields $\int_0^{\Omega} \mathrm{Re}\left[\sigma^{D}_{xx}(\omega)\right] d\omega = (\pi/2) D_{xx} = c\Delta_0 \mathcal{I}_x(\mu)$.

To illustrate the conservation of the optical weight $\mathcal{S}$ in Eq. (14), we plot the inter- and intraband (Drude) conductivity obtained from Eqs. (10) and (12) as a function of ω in Fig. 3(b). Note that as μ is tuned from $10 \to 20$ meV, parts of the red curve associated with interband conductivity become Pauli blocked. As expected from Eq. (14), the missing area is transferred to the intraband conductivity, and is captured as an increased Drude weight, D, and a larger (green) peak height for the intraband (Drude) conductivity in Fig. 3(b). Equation (14) is a powerful tool to analyze the low-energy spectroscopic features of the DSM surface states. Similar sum rule analyses have been used successfully to study two-dimensional surface states [21,22].

Before closing, we briefly outline the conditions that favor the observation of large surface absorption in DSMs. We note that the regime in which inter-Fermi arc transitions occur is limited by the bandwidth of the Fermi arc surface states $\sim v_x k_0$ which also directly determines the optical weight $\mathcal{S}$. Hence both wide k_0 as well as fast v_x are favorable. Additionally, when DSM bands possess particle-hole (p-h) asymmetry [e.g., via $\epsilon_{\mathbf{k}_{2\mathrm{D}}}$ in Eq. (3)], the particular distribution of occupied and unoccupied surface states that participate in absorption are directly impacted. For example, p-h asymmetry can induce additional Pauli blocking that can suppress the contribution of inter-Fermi arc transitions to surface absorption; for $\epsilon_{\mathbf{k}_{2\mathrm{D}}} \ll \Delta_{\mathbf{k}_{2\mathrm{D}}}$, the effects of p-h asymmetry are negligible.

In addition to the inter-Fermi arc transitions, and bulk-bulk interband transitions [17,18], we note that inter-Fermi arc bulk transitions may also occur [23]. These transitions will further add to the already large surface absorption from inter-Fermi arc transitions described above. However, we expect these depend sensitively on the details of the dispersion on the surface.

Fermi arc carriers can possess a strong light-matter interaction, characterized by a large optical conductivity, peaklike frequency dependence, as well as linear dichroism of inter-Fermi arc transitions. Importantly, Fermi arc carriers have a strikingly different optical response as compared with DSM bulk carriers. The delineated optical response between bulk and Fermi arc are a Hallmark of how spectral weight is spatially distributed between bulk and surface in DSMs, and can be used to characterize DSMs optically.

Acknowledgments. We thank Alex Frenzel and Mark Rudner for useful conversations. This work was supported by the Singapore National Research Foundation (NRF) under NRF fellowship Award No. NRF-NRFF2016-05.

[1] Z. J. Wang, Y. Sun, X. Q. Chen, C. Franchini, G. Xu, H. M. Weng, X. Dai, and Z. Fang, Phys. Rev. B **85**, 195320 (2012); Z. J. Wang, H. M. Weng, Q. S. Wu, X. Dai, and Z. Fang, *ibid.* **88**, 125427 (2013).

[2] B. J. Yang and N. Nagaosa, Nat. Commun. **5**, 4898 (2014).

[3] M. Neupane, S.-Y. Xu, R. Sankar, N. Alidoust, G. Bian, C. Liu, I. Belopolski, T.-R. Chang, H.-T. Jeng, H. Lin, A. Bansil, F. C. Chou, and M. Z. Hasan, Nat. Commun. **5**, 3786 (2014).

[4] S. Y. Xu, C. Liu, S. K. Kushwaha, R. Sankar, J. W. Krizan, I. Belopolski, M. Neupane, G. Bian, N. Alidoust, T. R. Chang,

H. T. Jeng, C. Y. Huang, W. F. Tsai, H. Lin, P. P. Shibayev, F. C. Chou, R. J. Cava, and M. Z. Hasan, Science **347**, 294 (2015).

[5] S. Borisenko, Q. Gibson, D. Evtushinsky, V. Zabolotnyy, B. Büchner, and R. J. Cava, Phys. Rev. Lett. **113**, 027603 (2014).

[6] M. Neupane, S. Y. Xu, N. Alidoust, R. Sankar, I. Belopolski, D. S. Sanchez, G. Bian, C. Liu, T. R. Chang, H. T. Jeng, B. K. Wang, G. Q. Chang, H. Lin, A. Bansil, F. C. Chou, and M. Z. Hasan, Phys. Rev. B **91**, 241114 (2015).

[7] S. Y. Xu, C. Liu, I. Belopolski, S. K. Kushwaha, R. Sankar, J. W. Krizan, T. R. Chang, C. M. Polley, J. Adell, T. Balasubramanian, K. Miyamoto, N. Alidoust, G. Bian, M. Neupane, H. T. Jeng, C. Y. Huang, W. F. Tsai, T. Okuda, A. Bansil, F. C. Chou, R. J. Cava, H. Lin, and M. Z. Hasan, Phys. Rev. B **92**, 075115 (2015).

[8] Z. K. Liu, B. Zhou, Y. Zhang, Z. J. Wang, H. M. Weng, D. Prabhakaran, S. K. Mo, Z. X. Shen, Z. Fang, X. Dai, Z. Hussain, and Y. L. Chen, Science **343**, 864 (2014); Z. K. Liu, J. Jiang, B. Zhou, Z. J. Wang, Y. Zhang, H. M. Weng, D. Prabhakaran, S.-K. Mo, H. Peng, P. Dudin, T. Kim, M. Hoesch, Z. Fang, X. Dai, Z. X. Shen, D. L. Feng, Z. Hussain, and Y. L. Chen, Nat. Mater. **13**, 677 (2014).

[9] S. Jeon, B. B. Zhou, A. Gyenis, B. E. Feldman, I. Kimchi, A. C. Potter, Q. D. Gibson, R. J. Cava, A. Vishwanath, and A. Yazdani, Nat. Mater. **13**, 851 (2014).

[10] A. Akrap, M. Hakl, S. Tchoumakov, I. Crassee, J. Kuba, M. O. Goerbig, C. C. Homes, O. Caha, J. Novák, F. Teppe, W. Desrat, S. Koohpayeh, L. Wu, N. P. Armitage, A. Nateprov, E. Arushanov, Q. D. Gibson, R. J. Cava, D. van der Marel, B. A. Piot, C. Faugeras, G. Martinez, M. Potemski, and M. Orlita, Phys. Rev. Lett. **117**, 136401 (2016).

[11] T. Liang, Q. Gibson, M. N. Ali, M. H. Liu, R. J. Cava, and N. P. Ong, Nat. Mater. **14**, 280 (2015).

[12] A. A. Burkov, Nat. Mater. **15**, 1145 (2016).

[13] M. Kargarian, M. Randeria, and Y. M. Lu, Proc. Natl. Acad. Sci. USA **113**, 8648 (2015).

[14] A. C. Potter, I. Kimchi, and A. Vishwanath, Nat. Commun. **5**, 5161 (2014).

[15] P. J. W. Moll, N. L. Nair, T. Helm, A. C. Potter, I. Kimchi, A. Vishwanath, and J. G. Analytis, Nature (London) **535**, 266 (2016).

[16] R. R. Nair, P. Blake, A. N. Grigorenko, K. S. Novoselov, T. J. Booth, T. Stauber, N. M. R. Peres, and A. K. Geim, Science **320**, 1308 (2008).

[17] P. E. C. Ashby and J. P. Carbotte, Phys. Rev. B **89**, 245121 (2014); D. Neubauer, J. P. Carbotte, A. A. Nateprov, A. Löhle, M. Dressel, and A. V. Pronin, *ibid.* **93**, 121202 (2016).

[18] See Supplemental Material at http://link.aps.org/supplemental/10.1103/PhysRevB.96.081410 for a discussion of DSM surface states and its low-energy effective Hamiltonian, other models of $\Delta_{\mathbf{k}_{2D}}$, interband transitions for the Dirac semimetal bulk states, and identity for $\mathcal{I}_x(\mu)$.

[19] Here we adopted a continuous gauge that $\phi_{\mathbf{k}_{2D}} \in [-\pi,\pi]$ with $\phi_{k_z=0} = 0$.

[20] While $\mathrm{Re}(\sigma_{xx})$ exhibits a peaklike frequency dependence, $\mathrm{Re}(\sigma_{zz})$ features only a small kink at $\hbar\omega/2 = \Delta_0$. This difference between $\mathrm{Re}(\sigma_{zz})$ and $\mathrm{Re}(\sigma_{xx})$ is due to the appearance of a factor of $(1-\bar{\omega}^{-2\zeta}\sin^2\nu)$ in the matrix element $|\mathcal{M}_z|^2$ which eliminates the divergence in $\rho(\omega,\nu) \sim (1-\bar{\omega}^{-2\zeta}\sin^2\nu)^{-1/2}$ at $\bar{\omega} \to 1$ and $\nu \to \pi/2$.

[21] D. N. Basov, M. M. Fogler, A. Lanzara, F. Wang, and Y. Zhang, Rev. Mod. Phys. **86**, 959 (2014).

[22] K. W. Post, B. C. Chapler, M. K. Liu, J. S. Wu, H. T. Stinson, M. D. Goldflam, A. R. Richardella, J. S. Lee, A. A. Reijnders, K. S. Burch, M. M. Fogler, N. Samarth, and D. N. Basov, Phys. Rev. Lett. **115**, 116804 (2015).

[23] For a discussion of surface-bulk scattering in Weyl semimetals, see E. V. Gorbar, V. A. Miransky, I. A. Shovkovy, and P. O. Sukhachov, Phys. Rev. B **93**, 235127 (2016).